Well-dispersed iron oxide stabilized Fe−N$_4$ active sites in porous N-doped carbon spheres as alternative superior catalyst for oxygen reduction

Xiaoyang Cheng [a], Puxuan Yan [a], Siwen Liu [a], Mancai Qian [a], Benzhi Wang [a], Zixia Wan [a], Jianniao Tian [a], Xing-Can Shen [a], Tayirjan Taylor Isimjan [b],[**], Xiulin Yang [a],[*]

[a] Key Laboratory for the Chemistry and Molecular Engineering of Medicinal Resources (Ministry of Education of China), College of Chemistry and Pharmacy, Guangxi Normal University, Guilin 541004, China
[b] Saudi Arabia Basic Industries Corporation (SABIC), King Abdullah University of Science and Technology (KAUST), Saudi Arabian

ARTICLE INFO

ABSTRACT

The fabrication of highly active oxygen reduction reaction (ORR) catalysts with strong anti-poisoning and durability at low cost is extremely desirable but still remains a great challenge. Herein, a novel hierarchically structured material of N-doped porous carbon spheres embedded with monodispersed Fe$_2$O$_3$ clusters (Fe$_2$O$_3$/NPCS) is constructed. The composition and microstructure of Fe$_2$O$_3$/NPCS are carefully characterized, and the existed Fe$_2$O$_3$-stabilized Fe−N$_4$ active sites for ORR are verified. The Fe$_2$O$_3$/NPCS catalyst exhibits a superior ORR activity with a positive half-wave potential of 0.95 V, showing an obvious around 90 mV positive-shift over commercial Pt/C (20 wt%). Additionally, the high ORR catalytic activity is also accompanied by a smaller Tafel slope of 45.3 mV decade^{-1} than Pt/C, implying a fast kinetics at high potentials. Furthermore, the high-active catalyst also demonstrates an outstanding anti-poisoning capacity and long-term durability. The excellent ORR activites are attributed to the synergistic effect between the rich Fe−N$_4$ active sites protected by Fe$_2$O$_3$ clusters, the porous structures facilitating electron transport as well as the electrolyte and oxygen diffusion.

Introduction

Development of rationally designed, cost-effective and highly active catalysts for oxygen reduction reaction (ORR) is one of the key steps to develop fuel cells and metal-air batteries for industrial application [1,2]. Due to the kinetically sluggish four-electron transfer processes and complicated intermediates, platinum (Pt) and Pt-based alloys are identified as the most promising catalysts for ORR application, but their high cost, long-term stability, and poor methanol tolerance are the main drawbacks [3,4]. Consequently, substantial efforts have been made recently to develop an alternative to overcome above disadvantages inherited by Pt based ORR catalysts [5,6].

One of the most promising systems showing continues progress is metal/nitrogen (M-N$_x$/C) supported by carbon

based materials (M = Co, Ni, Cu and Fe) (Scheme 1) prepared by high-temperature pyrolysis because of their high ORR activities [7−9]. Due to the binding mechanism with O_2, Co and Fe are the two better suitable metals than Ni and Cu [10]. Therefore, Co and Fe based M-N_x/C exhibit higher activities than that of Ni and Cu catalysts [11]. In general, the carbon supports are graphene, carbon nanotube, porous carbon, *etc* [12]. Furthermore, the carbon based supports provide high surface area, suitable pore size distribution and good electron conductivity [13]. The N-doped carbon support provides a unique nitrogen-centered electron-donor with a nitrogen modified adjacent carbon electron-acceptor which introduce the nucleophilic-electrophilic surface function while interacting with oxygen and the reaction intermediates [14,15]. The three main nitrogen-carbon species are pyridinic, pyrrolic and quaternary (graphitic) nitrogen [16] as shown in Scheme 1.

Although a significant progress over the years has been made on clarifying the actual mechanism of this system, the overall understanding is still limited due to the discrepancy of defining the active site. Some believe the coordination between the metal with nitrogen atoms is crucial to facilitate O_2 adsorption and provide favorable reaction intermediate [17,18]. The other studies suggesting that there is no direct involvement of metal except facilitating the growth of N-doped carbon with distinct surface features for oxygen reduction [19,20]. Moreover, the substantial reports on the metal free N−C catalysts on ORR [5,21]. Furthermore, the type of the nanoclusters, morphology of the support, precursor materials and synthesis procedures each can alter the ORR activities and stabilities significantly [22]. Nevertheless, the best performing noble metal free ORR catalyst system is still Fe−N_4/C prepared by high-temperature pyrolysis meaning Fe−N−C structure provides a better active site regarding ORR than that of N−C. However, these catalysts frequently suffer from poor stability owing to the metal leaching during the electrochemical reaction resulting in losing activity and membrane contamination [23]. Thus protecting the active site become the critical step for long-term application. In order to keep the activity of unstable Fe−N core and overall electrical conductivity of the catalyst, the protective encapsulation should permit an easy access to the active site while not affecting the overall dynamics of the catalyst.

Herein, we report a new approach of synthesizing N-doped porous carbon spheres (NPCS) embedded with Fe_2O_3 nanoclusters (Fe_2O_3/NPCS) through the high-temperature pyrolysis. The Fe_2O_3 nanoclusters are uniformly dispersed inside the spherical graphitic shell to provide indirect contact with active sites, which are well encapsulated by the polar graphitic shell. The catalytic performance of the Fe_2O_3/NPCS are optimized and systematically characterized by the X-ray diffraction patterns, Raman spectrum, thermal gravimetric, elemental analyzers, N_2 adsorption-desorption isotherms, scanning/transmission electron microscopy and X-ray photoelectron spectroscopy. Electrochemical analysis demonstrates that the Fe_2O_3/NPCS catalyst possesses a superior ORR activity with excellent stability to compare with the commercial Pt/C in the alkaline media. To the best of our knowledge, the Fe_2O_3/NPCS is the almost best performing ORR catalyst in alkaline condition so far. Therefore, the fabricated Fe_2O_3/NPCS catalyst shows a great potential to replace the Pt-based catalysts for ORR.

Experimental section

Materials

Ferrocene (Fe(C_5H_5)$_2$, 99%), cetyltrimethyl ammonium bromide (CTAB, 99%), melamine ($C_3H_6N_6$, ≥99.0%), dopamine hydrochloride ((HO)$_2C_6H_3CH_2CH_2NH_2$·HCl, 98%), acetone (CH_3COCH_3, ≥99.5%), anhydrous ethanol (C_2H_5OH, ≥99.7%). All the reagents were analytical reagent and used without further purification. Commercial Pt/C (20% for platinum) was purchased from Alfa Aesar. Iron phthalocyanine (FePc) was purchased from Acros organics. Nafion solution with *ca.* 5% of Nafion in the mixture of lower anhydrous ethanol and water was purchased from Alfa Aesar. The water was purified through a Millipore system.

Synthesis of Fe_2O_3-polydopamine (PDA) spheres

The Fe_2O_3-PDA spheres were prepared by a typical solvothermal method, where 0.75 g ferrocene and 0.1 g cetyltrimethyl ammonium bromide (CTAB) were ultrasonically
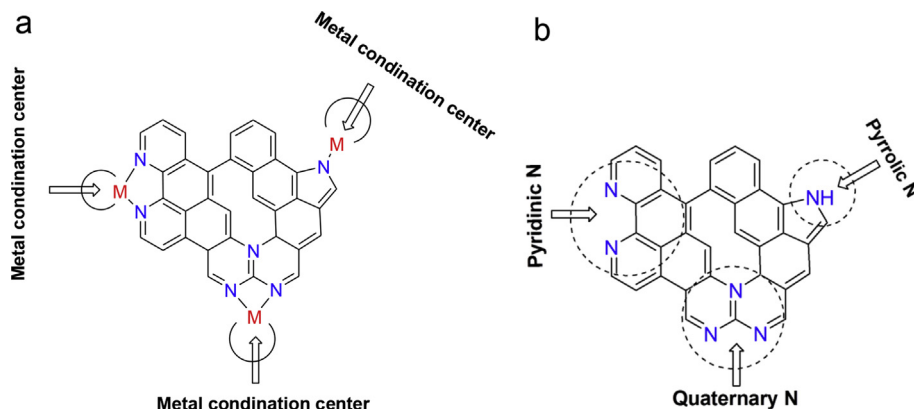
Scheme 1 − M-N_x/C catalyst for ORR application: (a) metal coordinated with N-doped carbon support and (b) N-doped carbon support.

dispersed into 65 mL acetone solution. Ten minutes later, 10 mL of 20 mg mL^{-1} dopamine hydrochloride in acetone solution was added dropwise into the above mixtures under continuous stirring at room temperature. Thirty minutes later, the resulted mixtures were poured into a Teflon-lined autoclave and heated at 200 °C for 24 h. The obtained precipitates were washed with ethanol and deionized (DI) water several times and then dried at 60 °C for 6 h. The final products were denoted as Fe_2O_3-PDA.

Synthesis of Fe_2O_3/NPCS and Fe_2O_3/PCS

For the preparation of series of Fe_2O_3/NPCS-T (T = 800, 900, 1000 and 1100 °C) catalysts, 200 mg of the as-prepared Fe_2O_3-PDA and melamine (mass ratio for 1/2) were evenly mixed by grinding. The resulting products were transferred into a porcelain boat and annealed at 250 °C under the N_2 atmosphere for 3 h. Then, it was further heated to a specific temperature (800, 900, 1000 or 1100 °C) with a heating rate of 5 °C min^{-1} and maintained at the temperature for 2 h. The as-obtained samples were denoted as Fe_2O_3/NPCS-800, 900, 1000 and 1100. Moreover, the different mass ratios of Fe_2O_3-PDA and melamine (1/1 and 1/3) were also used to prepare Fe_2O_3/NPCS-1000 by the similar process described above. For the comparison, the Fe_2O_3/PCS-1000 material was fabricated by direct calcination of Fe_2O_3-PDA at 250 °C for 3 h and subsequent at 1000 °C for 2 h under the N_2 atmosphere.

Characterization

Scanning electron microscopy (SEM, Quanta FEG 200, Holland) and transmission electron microscopy (TEM, JEOL, JEM-2100F) were used to investigate the morphologies and microstructures of the designed materials. Raman spectroscopy was acquired from an inVia confocal Raman microscope (Renishaw, England). X-ray powder diffraction (XRD) data was detected by a D/Max 2500 V PC with Cu Kαradiation from Rigaku. The chemical states of the samples were examined by X-ray photoelectron spectroscopy (XPS, model: JPS-9010 TR Photoelectron Spectrometer, Japan). The nitrogen content in the hybrid catalysts was analyzed by an elemental analyzer (PE2400II). The specific surface areas of the as-prepared products were measured on a Quantachrome Autosorb AS-1 instrument, and the pore size distributions were derived from the desorption branches of the isotherm with the Barrett-Joyner-Halenda (BJH) model. Thermal gravimetric measurement was made on a TGA/STA409 PC module with a rising temperature rate of 2.5 °C min^{-1} from 38 to 1000 °C under continuous O_2 flow.

Electrochemical measurements

The ORR activities of the as-prepared catalysts were studied by an electrochemical workstation of Biologic VMP3 with a typical three-electrode system in N_2— or O_2-saturated 0.1 M KOH electrolyte. A rotating disk (glassy carbon, GC) electrode with a diameter of 4 mm, Pt wire and Ag/AgCl electrode were used as working, counter and reference electrodes, respectively. The GC electrodes were polished with aluminum powder, cleaned in sulfuric acid, ethanol and water

subsequently for three times before use. The working electrode were prepared as follows: 2 mg of the as-synthesized catalyst powder was ultrasonically dispersed into 400 μL ($V_{water}:V_{2\text{-propanol}}:V_{Nafion} = 4:1:0.025$) aqueous solution. Thirty minutes later, 10 μL of the catalyst inks were pipetted onto several glassy carbon (GC) electrodes and further dried at room temperature. The loading of the catalyst on GC electrode is *ca.* 0.4 mg cm^{-2} and the Pt loading on GC electrode is *ca.* 0.08 mg cm^{-2}.

The cyclic voltammograms (CV) measurements were recorded in N_2— or O_2-saturated 0.1 M KOH electrolyte with a scan rate of 50 mV s^{-1}. The liner sweep voltammetry (LSV) curves were conducted at a scan rate of 10 mV s^{-1} with a rotating speed from 400 to 2500 rpm in O_2-saturated 0.1 M KOH. The chronoamperometric curves were operated at a constant potential of 0.56 V (vs. RHE) in O_2-saturated 0.1 M KOH. All potentials (vs. Ag/AgCl) in this work were calibrated to the RHE by the average CV curves of the two potentials at which the current crossed zero (0.960 V) was taken to be the thermodynamic potential in H_2-saturated 0.1 M KOH (Fig. S1). The result is lower than E(RHE) = E(Ag/AgCl) + 0.197 + 0.059 pH = E(Ag/AgCl) + 0.964 V. All curves were reported here without iR compensation and all the electrochemical tests were performed at room temperature (25 ± 1 °C).

The *Koutecky-Levich* (K-L) plots of all catalysts were created from LSV curves to evaluate the electron transfer number (n) and kinetic current density (J_K), in which the n per O_2 molecule and J_K in ORR can be collected according to the following equations [24]:

$$B = 0.62nFC_oD_0^{2/3}v^{-1/6} \tag{1}$$

$$1/J = 1/J_k + 1/J_L \tag{2}$$

$$1/J = 1/J_K + 1/B\omega_{1/2} \tag{3}$$

where J is the measured current density, J_K and J_L are the kinetic and diffusion-limited current densities. n is the electron transfer number per molecule of O_2, F is the Faraday constant (96485 C mol^{-1}), C_0 is the bulk concentration of oxygen (1.2×10^{-3} mol L^{-1}), D_0 is the diffusion coefficient of oxygen in the bulk solution (1.9×10^{-5} cm^2 s^{-1}), v is the kinematic viscosity ($v = 0.01$ cm^2 s^{-1}), and ω is the angular velocity of the disk ($\omega = 2\pi N$, N is the linear rotation speed).

Ring-rotated disk electrode (RRDE) test was also carried out on the Fe_2O_3/NPCS-1000 electrode with the rotating speed fixed at 1600 rpm. The corresponding electron transfer number (n) and H_2O_2 yield were calculated from the following equation:

$$H_2O_2(\%) = 200 \times \frac{\frac{I_R}{N}}{I_D + \frac{I_R}{N}} \tag{4}$$

The electron transfer number (n) was calculated from the following equation:

$$n = 4 \times \frac{I_D}{I_D + \frac{I_R}{N}} \tag{5}$$

Where I_D and I_R mean the disk and ring currents, respectively, n denotes the electron transfer number in the ORR performance test, and N is the collection efficiency (0.37).

Results and discussion

Synthesis strategy analysis

The schematic preparation of Fe_2O_3/NPCS materials at different temperatures are shown in Scheme 2. Firstly, the Fe_2O_3-PDA composite are obtained by a solvothermal decomposition in acetone solution, where ferrocene, dopamine hydrochloride, and CTAB are respectively used as iron precursor, carbon source, and structure directing agent. During the pyrolysis process, the ferrocene is gradually oxidized by oxygen resulted from acetone decomposition to form Fe_2O_3 species [25], which are subsequently coated by self-polymerized dopamine [26,27], thereof controlled the crystal growth of Fe_2O_3 effectively. Consequently, the ultra-small Fe_2O_3 clusters are uniformly dispersed in the carbon matrix. The resulting precipitate (Fe_2O_3-PDA) was filtered and calcinated with melamine under constant N_2 flow in the temperature range of 800–1100 °C for 2 h to obtain Fe_2O_3/NPCS. The optimal Fe_2O_3-PDA/melamine ratio prior to the calcination at 1000 °C regarding ORR activity is found to be 1:2. Note that Fe_2O_3/NPCS refers to calcined products at 1000 °C unless otherwise specified.

### Crystal structures, compositions and thermal analysis

The crystal structures of the obtained products are characterized by powder X-ray diffraction (XRD) patterns. As shown in Fig. 1a, the XRD pattern of Fe_2O_3/PCS exhibits three groups of crystalline-diffraction peaks, where the two peaks at ca. 26.1 and 40.9° are corresponding to the characteristic peaks of graphitic carbon (002) and (100) diffractions [28,29], the characteristic peaks at ca. 24.2, 33.2 and 49.5° are ascribed to the rhombohedral hematite (Fe_2O_3, JCPDS: 33–0664). The last group of peaks are assigned to the crystal planes of the cubic maghemite (Fe_2O_3, JCPDS: 39–1346) [30]. Interestingly, the diffraction pattern of graphitized carbon became almost invisible after pyrolysis under nitrogen indicating the graphitized carbon structure has been modified. Moreover, all other the diffraction patterns of Fe_2O_3 in the Fe_2O_3/NPCS become much weaker and

broader than those of Fe_2O_3/PCS indicating inhibition of the crystal growth and agglomeration of Fe_2O_3 resulted from N-doping. In addition, the effect of the high temperature on the crystal structure of the iron oxide species is also investigated (Fig. S2). The XRD results indicate that some of Fe_2O_3 species have been reduced to the FeO and Fe_3O_4 which is also confirmed by XPS.

Raman spectra are also used to analyze the structural information and the degree of the graphitization on the samples. As shown in Fig. 1b, the Raman shifts at 1345 and 1599 cm^{-1} are attributed to the D-band and G-band respectively, where the D-band stands for defect and G-band represents the crystallization degree of the sp^2 hybrid carbon atoms [31]. Therefore, the degree of the graphitization can be found quantitatively by the intensity ratio of the D to G bands (I_D/I_G). The I_D/I_G values are increased from 0.92 to 0.95 after N-doping indicating a higher level of defect formation. This phenomena results more nitrogen binding sites for the formation of Fe–N active site and subsequently improves the ORR performance. Although more defect can be resulted at the higher temperature (Fig. S3), the favorable catalyst configuration may also be altered thereof resulting in the decline of ORR activities. The 1000 °C is found to be the optimal annealing temperature.

The specific surface area and the porosity of Fe_2O_3/NPCS are also investigated by Brunauer-Emmett-Teller (BET) gas-sorption measurements (Fig. 1c). The N_2 adsorption-desorption isotherms at 77 K shows a type IV isotherm with a distinct hysteresis loop at relative pressures (P/P_o) of ca. 0.4 to 1.0 [30,32]. The BET specific surface area, pore volume and average pore size of Fe_2O_3/NPCS are ca. 592.0 $m^2\ g^{-1}$, 1.1 $m^3\ g^{-1}$ and 19.0 nm respectively. A highly active ORR performance is expected due to the high surface area and porosity [33].

The iron oxide content is measured by TG and DTG curves of Fe_2O_3/NPCS (Fig. 1d). The two distinct peaks at 65.4 and 484.5 °C in the temperature range of 38–1000 °C are associated with the loss of moisture and carbons, respectively. The total weight loss of ca. 54.9 wt % shows that the mass content of Fe_2O_3 species in the hybrid catalyst is ca. 45.1 wt %. Moreover, the N contents of the same samples after different annealing temperature are also analyzed at various temperatures. As
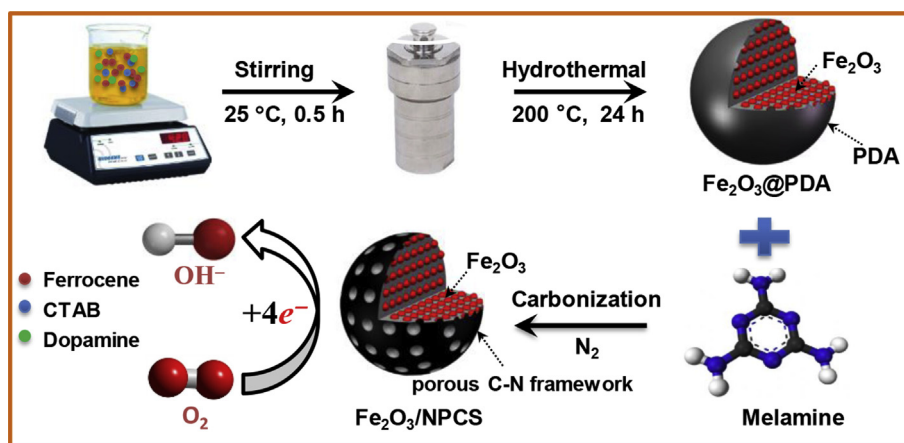
Scheme 2 – Schematic diagram of the reaction process for synthesizing Fe_2O_3/NPCS.

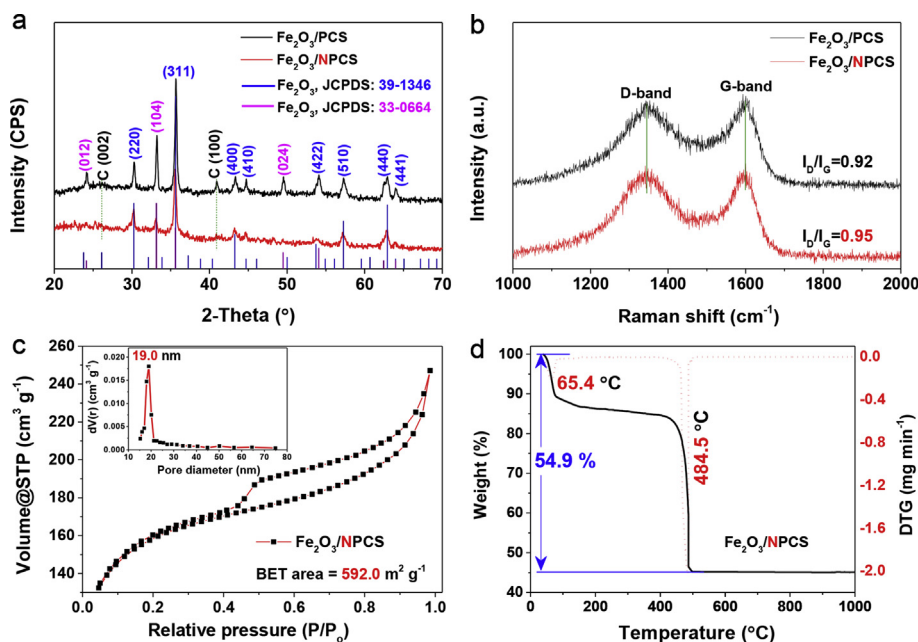Fig. 1 – (a) X-ray diffraction patterns and (b) Raman spectrum of Fe$_2$O$_3$/PCS and Fe$_2$O$_3$/NPCS. (c) Nitrogen adsorption–desorption isotherms with the pore size distribution curves by the BJH method (inset) of Fe$_2$O$_3$/NPCS. (d) Thermal gravimetric (TG) analysis and derivative thermal gravimetry (DTG) curves of Fe$_2$O$_3$/NPCS in O$_2$ atmosphere with a rising temperature rate of 2.5 °C min^{-1}.

expected, the N content in the hybrid catalysts decreases gradually with the increase of the calcination temperature meanwhile the N content increases with the increase of the amount of the nitrogen source (melamine) at the same calcination temperature (Table S1).

Microstructures analysis

Scanning electron microscopy (SEM), transmission electron microscopy (TEM) and high-resolution transmission electron microscopy (HRTEM) images provide insight into the morphologies and structures of Fe$_2$O$_3$-PDA and Fe$_2$O$_3$/NPCS. Fig. 2a shows a well-defined and uniformly distributed spheres with an average diameter of ca. 1.2 μm. The high-magnification SEM image shows that the surface of both spherical Fe$_2$O$_3$-PDA and Fe$_2$O$_3$/NPCS nanoclusters. The average gap between them is about 12.0 nm (Fig. 2a–b inset, Fig. S4a-4b). Fig. 2c (inset) exhibits well-defined lattice fringes with a lattice spacing of 0.48 nm, which is corresponding to the (111) plane of Fe$_2$O$_3$. This type of nano and macro porous structure creates a high level of porosity that is also proved by the TEM image (Fig. 2c) of Fe$_2$O$_3$/NPCS where the spheres are translucent. The high-resolution TEM shows that the average particle size of the Fe$_2$O$_3$ nanoclusters is ca. 4.2 nm, apart from some large agglomerations (Fig. S4c-4d). Moreover, the black pixels of Fe$_2$O$_3$ are evenly distributed throughout the structures, indicating the embedded Fe$_2$O$_3$ species are well dispersed in the porous structure of the N-doped carbon sphere. Additionally, the HAADF-STEM and corresponding elemental mapping images demonstrate the uniform distribution of C, N, Fe and O in the Fe$_2$O$_3$/NPCS, displaying nano level of dispersions of both N and Fe$_2$O$_3$ species in the hybrid material.

XPS analysis

X-ray photoelectron spectroscopy (XPS) is further employed to probe the surface compositions of Fe$_2$O$_3$/PCS and F$_2$O$_3$/NPCS, where the C, O, and Fe are detected in both samples, while the N is only observed in the Fe$_2$O$_3$/NPCS material (Fig. S5a), suggesting a successful N-doping into the porous carbon matrix. Note that the core level of C 1s is deconvoluted into C=C, C–C and C–O at 284.0, 284.8 and 286.0 eV as correction standard (Fig. S5b) [34,35]. The high temperature is proven to enhance ORR activity owing to the formation of iron ion coordinated by nitrogen (Fe–N$_4$) active site structure that bridges the two adjacent graphitic crystallite [36]. The formation of bridging structure is mostly possible with either pyridinic or quaternary (graphitic) nitrogen heteroatoms. The high-resolution N 1s spectrum of the Fe$_2$O$_3$/NPCS reveals that peaks at 398.2, 399.9, 401.1 and 403.7 eV are corresponding to the pyridinic-N, the pyrrolic-N, graphitic-N and the oxidized-N, respectively (Fig. 3a) [37]. Although some reports show the improved ORR performance upon N doping, the actual mechanism is still not very clear [38]. However, it is widely accept that enhanced ORR activity has something to do with Lewis-basicity of the nitrogen next to the pyridinic N [39]. Therefore, the high pyridinic N content (44.3%, Table S2) is a direct indication of high numbers of active sites in Fe$_2$O$_3$/NPCS. Apart from the positive effect of high-density Fe–N$_4$ bridging structure, the other reason to improve ORR activity is using heat treatment to positively shift the redox potential of the central iron ions thus offering a higher number of Fe(II) active sites [11]. As shown in Fig. 3b, the high-resolution Fe 2p spectra of Fe$_2$O$_3$/PCS and Fe$_2$O$_3$/NPCS are deconvoluted into four pairs of peaks [40]. Both Fe(III) and Fe(II) oxides are described as high spin, leading to
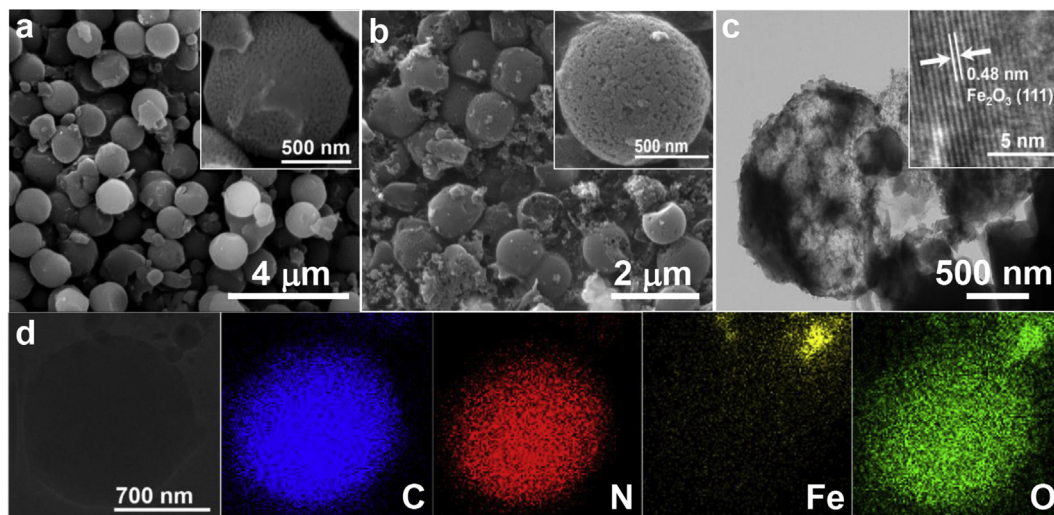
Fig. 2 – Typical SEM and high-magnification SEM images (inset) of (a) Fe_2O_3-PDA and (b) Fe_2O_3/NPCS. (c) TEM and high-resolution TEM images (inset) of Fe_2O_3/NPCS. (d) HAADF-STEM image of Fe_2O_3/NPCS and corresponding element mapping images of C (blue), N (red), Fe (yellow) and O (green). (For interpretation of the references to colour in this figure legend, the reader is referred to the Web version of this article.)
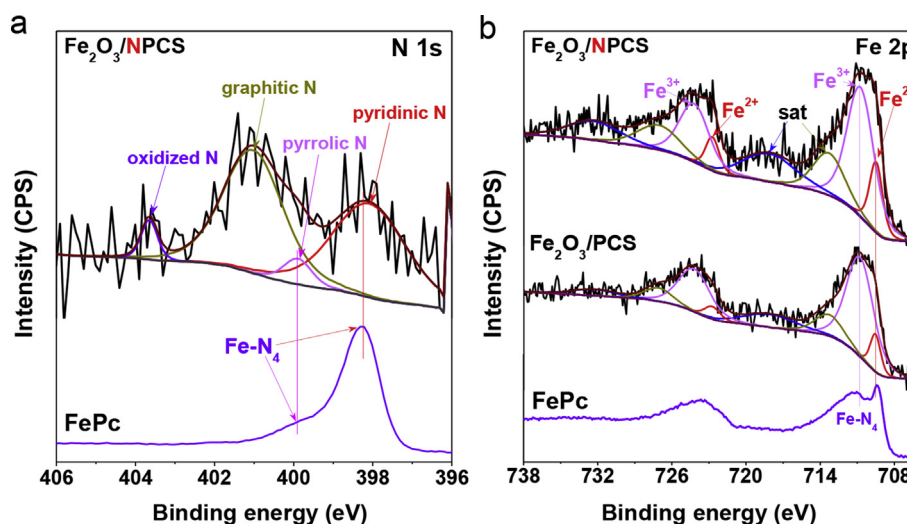

Fig. 3 – High-resolution XPS spectra of (a) N 1s region of Fe_2O_3/NPCS and commercial FePc. (b) Fe 2p regions of Fe_2O_3/NPCS, Fe_2O_3/PCS and FePc.

complex multi-split Fe 2P spectra. In the Fe $2p_{3/2}$ region, the peaks at 709.5 and 710.8 eV are assigned to Fe(II) and Fe(III) species, and the rest of two peaks are located as satellite peaks accordingly [41]. The content of Fe(II) increased noticeably in the Fe_2O_3/NPCS (21.0%) indicating a higher concentration of Fe(II)—N_4 active sites compare to that of Fe_2O_3/PCS (12.8%), therefore, a higher ORR activity is expected.

Electrochemical analysis

Linear sweep voltammetry (LSV) measurements are performed to test the electrochemical activity of Fe_2O_3/NPCS, together with Fe_2O_3/PCS and commercial Pt/C with the rotation disk electrode (RDE) at 1600 rpm with a scan rate of 10 mV s^{-1}. As shown in Fig. 4a, the LSV curve of Fe_2O_3/NPCS

catalyst exhibits superior ORR activity with a positive onset potential (E_{onset}) of 1.06 V, half-wave potential ($E_{1/2}$) of 0.95 V and the peak potential (E_p) of 0.86 V in 0.1 M KOH. All these parameters are significantly higher than that of Pt/C (20 wt %), Fe_2O_3/PCS and series of Fe_2O_3/NPCS-based catalysts synthesized by different methods (Fig. S6). Notably, the $E_{1/2}$ of the optimized Fe_2O_3/NPCS catalyst shows the significant positive shift of 90 mV over Pt/C (20 wt %) catalyst which is the highest catalysts reported so far. In addition, the Fe_2O_3/NPCS catalyst reveals a superior ORR performance than those of the previously reported works (Table S3). Furthermore, the superior ORR activity of Fe_2O_3/NPCS is further verified by the Tafel plots obtained from the polarization curves with a slope value of 45.3 mV dec^{-1}, which is around 6% lower than that of commercial 20 wt% Pt/C (48.4 mV dec^{-1}) and Fe_2O_3/PCS (58.7 mV
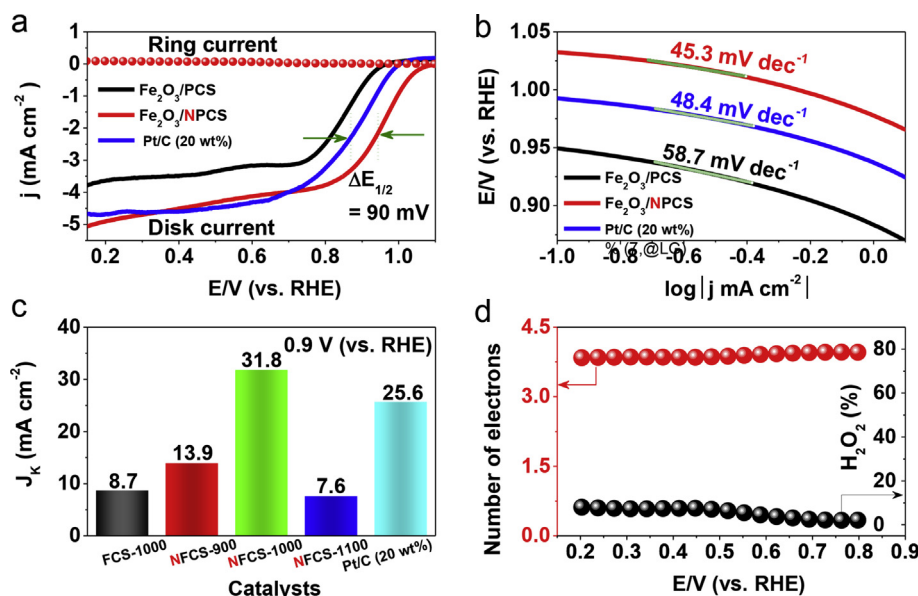
Fig. 4 – (a) LSV curves and (b) corresponding Tafel plots of Fe_2O_3/PCS, Fe_2O_3/NPCS and commercial Pt/C catalysts with a rotation rate of 1600 rpm in O_2-saturated 0.1 M KOH solution. (c) Summarized J_K of different catalysts. (d) Electron transfer number and H_2O_2 yield of Fe_2O_3/NPCS at a rotation rate of 1600 rpm.

dec^{-1}). The lower Tafel slope implies a faster kinetics due to the higher J_K (Fig. 4b) [42].

The LSV curves for ORR on the Fe_2O_3/NPCS at different rotation speeds are displayed in Fig. S7. The limiting current density in the LSV curves increases rapidly with the increase of rotation speed due to a smaller diffusion layer at high speeds. According to the Koutecky–Levich (K–L) equation, the K–L plots of Fe_2O_3/NPCS obtained from the LSV curves exhibit a good linear relationship showing a first-order reaction kinetics with the electron transfer numbers (n) of ca. 3.97 in the potential range of 0.4–0.8 V (Fig. S7 inset). These results indicate that the ORR mechanism of Fe_2O_3/NPCS follows the four-electron pathway (Fig. S8) [43]. Besides, the kinetic current density (J_K) of Fe_2O_3/NPCS is determined to be 31.8 mA cm^{-2} (at 0.9 V) by the K–L equation, which is nearly 3.6- and 1.3-fold higher than that of Fe_2O_3/PCS and Pt/C catalysts (Fig. 4c), respectively.

The ORR four-electron pathways were also determined by RRDE measurement. The percentage of peroxide species with respect to the total oxygen reduction products and the electron transfer number (n) are calculated from the RRDE curves, and the results are shown in Fig. 4d. The average yield of peroxide species for the Fe_2O_3/NPCS catalyst was about 5.0% over the measured potential range from 0.2 to 0.8 V. The electron transfer number calculated from the RRDE measurements was over 3.85 for Fe_2O_3/NPCS. The results indicated that an approximate four electron mechanism on Fe_2O_3/NPCS, which are consistent with the RDE test.

To investigate the stability of Fe–N$_4$ active sites, thiocyanate (SCN$^-$) ions introduced to monitor the effect of SCN$^-$ on ORR activity. In general, the SCN$^-$ tend to poison the Fe–N$_4$ active sites [44,45]. As shown in Fig. 5a, there is a negligible influence on the ORR performance of Fe_2O_3/NPCS catalyst after KSCN was added into the electrolyte, indicating that the Fe–N$_4$ species are very well protected and stable.

Furthermore, chronoamperometry measurements are also applied for investigating methanol resistance of Fe_2O_3/NPCS and commercial Pt/C (20 wt %) catalysts. After adding 3.0 M methanol at 200 s (Fig. 5b), almost no change is observed in the relative current curve of Fe_2O_3/NPCS catalyst. In contrast, a none reversible sharp decay in the relative current of Pt/C (20 wt %) is observed owing to the electrochemical oxidation of methanol on Pt surface [46]. The superior performance of Fe_2O_3/NPCS is attributed to the C–N shell-coated iron oxide stabilized Fe–N$_4$ active sites avoiding direct contact with methanol.

Besides the catalytic activity, the long-term stability is another vital factor for the large-scale application of fuel cell technologies. In order to assess the stability of the catalyst, we initially investigated the electrochemical durability of the Fe_2O_3/NPCS by cycling the potential between 0.6 V and 1.2 V (vs. RHE) in O_2-staurated 0.1 M KOH at 50 mV s^{-1} [47]. As shown in Fig. 5c, the $E_{1/2}$ of Fe_2O_3/NPCS shows a small negative shift of ~16 mV after 2000 cycles. In contrast, the $E_{1/2}$ of the Pt/C (20 wt %) catalyst show obvious negative shift (~66 mV) under the same conditions (Fig. 5d). Meanwhile, the chronoamperometry test was also performed at 0.6 V in O_2-saturated 0.1 M KOH solution with a rotation rate of 1600 rpm for 20 h. As displayed in Fig. 5e, the Fe_2O_3/NPCS catalyst maintained a higher and stable initial and final relative current than those of commercial Pt/C (20 wt %). Notably, the Fe_2O_3/NPCS catalyst keeps ca. 82.4% activity, which is significantly higher than that of the commercial Pt/C (20 wt %, retention ca. 63.3%) after 20 h. The high catalytic activity and long-term stability are mostly related to the two factors namely well-protected Fe–N$_4$ active sites and the porous sphere structures. The porous carbon frame not only creates mechanical integrity and good conductivity but also manifests a high degree of accessibility towards the active sites.
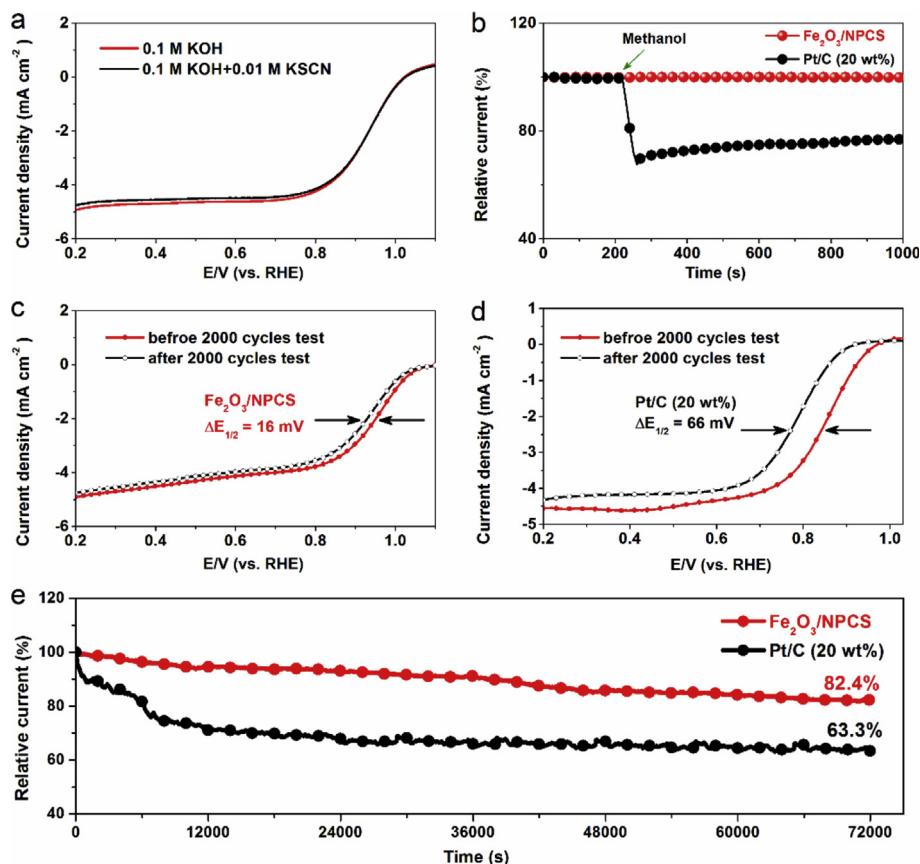
Fig. 5 − (a) LSV curves of SCN^- poison measurement on Fe_2O_3/NPCS before and after adding 3.0 mL of 10 mM KSCN into O_2-saturated 0.1 M KOH (40 mL). (b) Chronoamperometric response of Fe_2O_3/NPCS and Pt/C (20 wt %) catalysts at 0.60 V with addition of 2.0 mL of 3 M methanol at *ca.* 200 s. LSV curves of (c) Fe_2O_3/NPCS and (d) Pt/C for ORR in O_2-saturated 0.1 M KOH before and after 2000 cycles at a scan rate of 50 mV s^{-1} between 0.6 V and 1.2 V vs RHE. (d) Long-term durability test of Fe_2O_3/NPCS and Pt/C for 20 h in O_2-saturated 0.1 M KOH at 1600 rpm.

Catalytic mechanism analysis

To further explain the enhanced ORR performance of Fe_2O_3/NPCS catalyst, we proposed a four-step ORR mechanism in the alkaline solution as shown in Scheme 3. Step 1: an O_2 molecule is adsorbed on the active site of Fe−N_4 to form O_2^* [O_2(g) + * → O_2^*] [48]. Step 2: the O_2^* is reduced to OOH* [O_2^* + H_2O(l) + e^- →

OOH* + OH$^-$] [39]. Step 3: the O−O bond of OOH* is broken to form O* [OOH* + e^- → O* + OH$^-$] which is reduced spontaneously by the adsorbed H_2O to form *OH at the active site [O* + H_2O(l) + e^- → OH* + OH$^-$] [49]. Step 4: the surface adsorbed *OH dissolves as OH$^-$ species and leaves the surface [OH* + e^- → OH$^-$ + *].
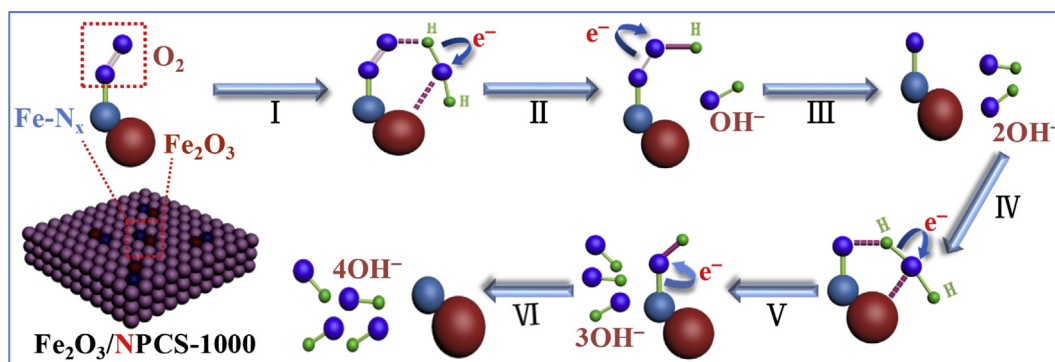
Scheme 3 − The proposed catalytic mechanism of Fe_2O_3/NPCS catalyst for ORR in alkaline media.

Conclusions

In summary, three-dimensional porous N-doped carbon spheres embedded with evenly dispersed Fe_2O_3 nanoclusters (Fe_2O_3/NPCS) has been synthesized by direct calcination of the mixture of Fe_2O_3-PDA microspheres and melamine. The Fe_2O_3-PDA microspheres are fabricated by a facile *in-situ* dopamine polymerization method. The formed Fe_2O_3/NPCS catalyst possesses a high specific surface area (*ca.* 592.0 m^2 g^{-1}) and Fe_2O_3 nanoclusters content (*ca.* 45.1 wt %). The both XRD and XPS analysis disclose the highest content of Fe(II)—N_4 species is estimated in the most active ORR catalyst (Fe_2O_3/NPCS) and the well protected Fe—N_4 active sites are inert to SCN^-. Electrochemical studies reveal that the Fe_2O_3/NPCS exhibits a superior electrochemical activity toward ORR compared to the state-of-the-art Pt/C catalyst, including positive onset potential (1.05 V), high half-wave potential (0.95 V), high kinetic current density (31.8 mA cm^{-2} at 0.7 V) and low Tafel slope (45.3 mV dec^{-1}). Meanwhile, the Fe_2O_3/NPCS catalyst also demonstrates an outstanding long-term stability and methanol tolerance ability during the ORR measurement. The superior ORR activity and stability of Fe_2O_3/NPCS catalyst as compared to the commercial Pt/C could be attributed to the synergic effects of (1) Fe—N_4 active sites that protected by iron oxide/N—C shell; (2) the highly porous and well-defined spherical outer shell permits the electron tunneling as well as the oxygen diffusion. In conclusion, this work demonstrates a simple protection method of Fe—N_4 active sites through iron oxide/N—C encapsulation. This facile approach may open a door to developing Pt-free catalyst for the commercial application.

Appendix A. Supplementary data

Supplementary data to this article can be found online at https://doi.org/10.1016/j.ijhydene.2019.03.068.

REFERENCES

[1] He W, Jiang C, Wang J, Lu L. High-rate oxygen electroreduction over graphitic-N species exposed on 3D hierarchically porous nitrogen-doped carbons. Angew Chem Int Ed 2014;53:9503—7.

[2] Kulkarni Ambarish, Siahrostami Samira, Patel Anjli, Nørskov Jens K. Understanding catalytic activity trends in the oxygen reduction reaction. Chem Rev 2018;118:2302—12.

[3] Cao R, Thapa R, Kim H, Xu X, Gyu Kim M, Li Q, Park N, Liu M, Cho J. Promotion of oxygen reduction by a bio-inspired tethered iron phthalocyanine carbon nanotube-based catalyst. Nat Commun 2013;4:2076.

[4] Huang Lei, Jiang Zheng, Gong Wenhao, Wang Zhen, Shen Pei Kang. Two-step etching fabrication of tunable ternary rhombic dodecahedral nanoframes for enhanced oxygen reduction electrocatalysis. J Power Sources 2018;406:42—9.

[5] Liu YL, Shi CX, Xu XY, Sun PC, Chen TH. Nitrogen-doped hierarchically porous carbon spheres as efficient metal-free electrocatalysts for an oxygen reduction reaction. J Power Sources 2015;283:389—96.

[6] Luo Lai-Ming, Zhan Wei, Zhang Rong-Hua, Chen Di, Hu Qing-Yun, Guo Yi-Fei, Zhou Xin-Wen. Ternary CoAuPd and binary AuPd electrocatalysts for methanol oxidation and oxygen reduction reaction: enhanced catalytic performance by surface reconstruction. J Power Sources 2019;412:142—52.

[7] Hoque Mahfuzul, Zhang Shiguo, Thomas Morgan L, Li Zhe, Suzuki Soma, Ando Ayumi, Yanagi Masato, Kobayashi Yoshio, Dokko Kaoru, Watanabe Masayoshi. Simple combination of a protic salt and an iron halide: precursor for a Fe, N and S co-doped catalyst for the oxygen reduction reaction in alkaline and acidic media. J Mater Chem A 2018;6:1138—49.

[8] Khandelwal Mahima, Chandrasekaran Sundaram, Hur Seung Hyun, Chung Jin Suk. Chemically controlled in-situ growth of cobalt oxide microspheres on N,S-co-doped reduced graphene oxide as an efficient electrocatalyst for oxygen reduction reaction. J Power Sources 2018;407:70—83.

[9] Liu Yuchuan, Huang Baobing, Zhang Xuefei, Huang Xing, Xie Zailai. In-situ fabrication of nitrogen-doped carbon nanosheets containing highly dispersed single iron atoms for oxygen reduction reaction. J Power Sources 2019;412:125—33.

[10] Han Ce, Li Qun, Wang Dewen, Lu Qingqing, Xing Zhicai, Yang Xiurong. Cobalt sulfide nanowires core encapsulated by a N, S codoped graphitic carbon shell for efficient oxygen reduction reaction. Small 2018;14:1703642.

[11] He Wenhui, Wang Ying, Jiang Chunhuan, Lu Lehui. Structural effects of a carbon matrix in non-precious metal O_2-reduction electrocatalysts. Chem Soc Rev 2016;45:2396—409.

[12] Elumeeva Karina, Kazakova Mariya A, Morales Dulce Maria, Medina Danea, Selyutin Alexander, Golubtsov Georgiy, Ivanov Yurii, Kuznetzov Vladimir, Chuvilin Andrey, Antoni Hendrik, Muhler Martin, Schuhmann Wolfgang, Masa Justus. Bifunctional oxygen reduction/oxygen evolution activity of mixed Fe/Co oxide nanoparticles with variable Fe/Co ratios supported on multiwalled carbon nanotubes. ChemSusChem 2018;11:1204—14.

[13] An Li, Jiang Ning, Li Biao, Hua Shixin, Fu Yutong, Liu Jiaxi, Hao Wei, Xia Dingguo, Sun Zaicheng. A highly active and durable iron/cobalt alloy catalyst encapsulated in N-doped graphitic carbon nanotubes for oxygen reduction reaction by a nanofibrous dicyandiamide template. J Mater Chem A 2018;6:5962—70.

[14] Gong K, Du F, Xia Z, Durstock M, Dai L. Nitrogen-doped carbon nanotube arrays with high electrocatalytic activity for oxygen reduction. Science 2009;323:760—4.

[15] Wu Dan, Zhang Zhonghai. Simultaneous non-metal doping and cocatalyst decoration for efficient photoelectrochemical water splitting on hematite photoanodes. Electrochim Acta 2018;282:48—55.

[16] Yadav Roshni, Dixit CK. Synthesis, characterization and prospective applications of nitrogen-doped graphene: a short review. J Sci Adv Mater Devices 2017;2:141—9.

[17] Holby Edward F, Wu Gang, Zelenay Piotr, Taylor Christopher D. Structure of Fe—n_x—C defects in oxygen reduction reaction catalysts from first-principles modeling. J Phys Chem C 2014;118:14388—93.

[18] Gao F, Zhao GL, Wang Z, Bagayoko D, Liu DJ. Catalytic reaction on FeN$_4$/C site of nitrogen functionalized carbon nanotubes as cathode catalyst for hydrogen fuel cells. Catal Commun 2015;62:79−82.

[19] Matter PH, Wang E, Millet JM, Ozkan US. Characterization of the iron phase in CN$_x$-based oxygen reduction reaction catalysts. J Phys Chem C 2007;111:1444−50.

[20] Strickland Kara, Miner Elise, Jia Qingying, Tylus Urszula, Ramaswamy Nagappan, Liang Wentao, Sougrati Moulay-Tahar, Jaouen Frédéric, Mukerjee Sanjeev. Highly active oxygen reduction non-platinum group metal electrocatalyst without direct metal−nitrogen coordination. Nat Commun 2015;6:7343.

[21] Lee CH, Jun B, Lee SU. Metal-free oxygen evolution and oxygen reduction reaction bifunctional electrocatalyst in alkaline media: from mechanisms to structure-catalytic activity relationship. ACS Sustain Chem Eng 2018;6:4973−80.

[22] Chen Zhongwei, Higgins Drew, Yu Aiping, Zhang Lei, Zhang Jiujun. A review on non-precious metal electrocatalysts for PEM fuel cells. Energy Environ Sci 2011;4:3167−92.

[23] Liu R, Wu D, Feng X, Müllen K. Nitrogen-doped ordered mesoporous graphitic arrays with high electrocatalytic activity for oxygen reduction. Angew Chem Int Ed 2010;49:2565−9.

[24] Thanh TD, Chuong ND, Balamurugan J, Van Hien H, Kim NH, Lee JH. Porous hollow-structured LaNiO$_3$ stabilized N,S-codoped graphene as an active electrocatalyst for oxygen reduction reaction. Small 2017;13:1701884.

[25] Xu Xijun, Liu Jun, Liu Zhengbo, Shen Jiadong, Hu Renzong, Liu Jiangwen, Ouyang Liuzhang, Zhang Lei, Zhu Min. Robust pitaya-structured pyrite as high energy density cathode for high-rate lithium batteries. ACS Nano 2017;11:9033−40.

[26] Xu Li Qun, Jing Yang Wen, Neoh Koon-Gee, Kang En-Tang, Dong Fu Guo. Dopamine-induced reduction and functionalization of graphene oxide nanosheets. Macromolecules 2010;43:8336−9.

[27] Shultz Michael D, Ulises Reveles J, Khanna Shiv N, Carpenter Everett E. Reactive nature of dopamine as a surface functionalization agent in iron oxide nanoparticles. J Am Chem Soc 2007;129:2482−7.

[28] Tang Tingting, Gan Qiuping, Guo Xiaohui, Dong Hailin, Zhang Jifang, Zhao Yanchun, Tian Jianniao, Yang Xiulin. A hybrid catalyst of Pt/CoNiO$_2$ on carbon nanotubes and its synergetic effect towards remarkable ethanol electro-oxidation in alkaline media. Sustain Energ Fuels 2018;2:229−36.

[29] Gan Qiuping, Cheng Xiaoyang, Chen Judan, Wang Dongsheng, Wang Benzhi, Tian Jianniao, Taylor Isimjan Tayirjan, Yang Xiulin. Temperature effect on crystallinity and chemical states of nickel hydroxide as alternative superior catalyst for urea electrooxidation. Electrochim Acta 2019;301:47−54.

[30] Yang Xiulin, Wang Xueyun, Feng Yongqiang, Zhang Guoqiang, Wang Taishan, Song Weiguo, Shu Chunying, Jiang Li, Wang Chunru. Removal of multifold heavy metal contaminations in drinking water by porous magnetic Fe$_2$O$_3$@AlO(OH) superstructure. J Mater Chem A 2013;1:473−7.

[31] Zhao Yanchun, Yang Xiulin, Zhan Lu, Ou Shengju, Tian Jianniao. High electrocatalytic activity of PtRu nanoparticles supported on starch-functionalized multi-walled carbon nanotubes for ethanol oxidation. J Mater Chem 2011;21:4257−63.

[32] Wang Dongsheng, Liu Siwen, Gan Qiuping, Tian Jianniao, Taylor Isimjan Tayirjan, Yang Xiulin. Two-dimensional nickel hydroxide nanosheets with high-content of nickel(III) species towards superior urea electro-oxidation. J Electroanal Chem 2018;829:81−7.

[33] Hu Enlai, Yu Xin-Yao, Chen Fang, Wu Yadan, Hu Yong, Lou Xiong Wen. Graphene layers-wrapped Fe/Fe$_5$C$_2$ nanoparticles supported on N-doped graphene nanosheets for highly efficient oxygen reduction. Adv Energy Mater 2018;8:1702476.

[34] Wu Chongbei, Zhang Jifang, Guo Jingya, Sun Linxin, Ming Jun, Dong Hailin, Zhao Yanchun, Tian Jianniao, Yang Xiulin. Ceria-induced strategy to tailor Pt atomic clusters on cobalt−nickel oxide and the synergetic effect for superior hydrogen generation. ACS Sustain Chem Eng 2018;6:7451−7.

[35] Zeng Yikui, Tian SiSi, Wang Dongsheng, Dong Hailin, Cheng Xiaoyang, Zhao Yanchun, Tian Jianniao, Yang Xiulin. Facile synthesis of polyhedral Pd nanocrystals as a highly active and methanol-tolerant electrocatalyst for oxygen reduction. ChemistrySelect 2017;2:9291−7.

[36] Kramm UI, Abs-Wurmbach I, Herrmann-Geppert I, Radnik J, Fiechter S, Bogdanoff P. Influence of the electron-density of FeN$_4$-centers towards the catalytic activity of pyrolyzed FeTMPPCl-based ORR-electrocatalysts. J Electrochem Soc 2011;158:B69−78.

[37] Wu Chongbei, Guo Jingya, Zhang Jifang, Zhao Yanchun, Tian Jianniao, Taylor Isimjan Tayirjan, Yang Xiulin. Palladium nanoclusters decorated partially decomposed porous ZIF-67 polyhedron with ultrahigh catalytic activity and stability on hydrogen generation. Renew Energy 2019;136:1064−70.

[38] Cao Lei, Li Zhen-huan, Gu Yu, Li Dao-hao, Su Kun-mei, Yang Dong-jiang, Cheng Bo-wen. Rational design of N-doped carbon nanobox-supported Fe/Fe$_2$N/Fe$_3$C nanoparticles as efficient oxygen reduction catalysts for Zn-air batteries. J Mater Chem A 2017;5:11340−7.

[39] Guo Donghui, Shibuya Riku, Akiba Chisato, Saji Shunsuke, Kondo Takahiro, Nakamura Junji. Active sites of nitrogen-doped carbon materials for oxygen reduction reaction clarified using model catalysts. Science 2016;351:361−5.

[40] Jiang Mengpei, Wu Hongjun, Li Zhida, Ji Deqiang, Li Wei, Liu Yue, Yuan Dandan, Wang Baohui, Zhang Zhonghai. Highly selective photoelectrochemical conversion of carbon dioxide to formic acid. ACS Sustain Chem Eng 2018;6:82−7.

[41] Xin Yanmei, Kan Xiang, Gan Li-Yong, Zhang Zhonghai. Heterogeneous bimetallic phosphide/sulfide nanocomposite for efficient solar-energy-driven overall water splitting. ACS Nano 2017;11:10303−12.

[42] Guo Jianing, Li Yang, Cheng Yuanhui, Dai Liming, Xiang Zhonghua. Highly efficient oxygen reduction reaction electrocatalysts synthesized under nanospace confinement of metal−organic framework. ACS Nano 2017;11:8379−86.

[43] Yang Yang, Mao Kaitian, Gao Shiqi, Huang Hao, Xia Guoliang, Lin Zhiyu, Jiang Peng, Wang Changlai, Wang Hui, Chen Qianwang. O-, N-Atoms-Coordinated Mn cofactors within a graphene framework as bioinspired oxygen reduction reaction electrocatalysts. Adv Mater 2018;30:1801732.

[44] Wang Qiang, Zhou Zhi-You, Lai Yu-Jiao, You Yong, Liu Jian-Guo, Wu Xia-Ling, Terefe Ephrem, Chen Chi, Song Lin, Rauf Muhammad, Tian Na, Sun Shi-Gang. Phenylenediamine-based FeN$_x$/C catalyst with high activity for oxygen reduction in acid medium and its active-site probing. J Am Chem Soc 2014;136:10882−5.

[45] Jiang Wen-Jie, Gu Lin, Li Li, Zhang Yun, Zhang Xing, Zhang Lin-Juan, Wang Jian-Qiang, Hu Jin-Song, Wei Zidong, Wan Li-Jun. Understanding the high activity of Fe−N−C electrocatalysts in oxygen reduction: Fe/Fe$_3$C nanoparticles

boost the activity of Fe—n_x. J Am Chem Soc 2016;138:3570—8.

[46] Kone Issa, Xie Ao, Tang Yang, Chen Yu, Jia Liu, Chen Yongmei, Sun Yanzhi, Yang Xiaojin, Wan Pingyu. Hierarchical porous carbon doped with iron/nitrogen/sulfur for efficient oxygen reduction reaction. ACS Appl Mater Interfaces 2017;9:20963—73.

[47] Odedairo T, Yan X, Ma J, Jiao Y, Yao X, Du A, Zhu Z. Nanosheets Co3O4 interleaved with graphene for highly efficient oxygen reduction. ACS Appl Mater Interfaces 2015;7:21373—80.

[48] Liu Shizhong, White Michael G, Liu Ping. Mechanism of oxygen reduction reaction on Pt(111) in alkaline solution: importance of chemisorbed water on surface. J Phys Chem C 2016;120:15288—98.

[49] Chen Yuanjun, Ji Shufang, Wang Yanggang, Dong Juncai, Chen Wenxing, Li Zhi, Shen Rongan, Zheng Lirong, Zhuang Zhongbin, Wang Dingsheng, Li Yadong. Isolated single iron atoms anchored on N-doped porous carbon as an efficient electrocatalyst for the oxygen reduction reaction. Angew Chem Int Ed 2017;56:6937—41.